Chemical Science

ROYAL SOCIETY OF CHEMISTRY

EDGE ARTICLE

View Article Online
View Journal

Cite this: DOI: 10.1039/d6sc02881k

All publication charges for this article have been paid for by the Royal Society of Chemistry

Dynamic pendulum strategy enables both anti-quenching and fast spin flipping for efficient blue multiple-resonance thermally activated delayed fluorescence emitters

Xiangqin Gan,[a] Bitian Chen,[ab] Jia-Qi Li,[c] Han Si,*[a] Ning Sun,[d] Guoyun Meng,*[a] Xian-Kai Chen,*[c] Liming Ding,[f] Zheng-Hong Lu[de] and Junqiao Ding*[ab]

Multiple-resonance thermally activated delayed fluorescence (MR-TADF) emitters have attracted considerable interest due to their superiority in high-resolution organic light-emitting diodes (OLEDs), but suffer from severe aggregation-caused quenching and slow reverse intersystem crossing. Herein, a dynamic pendulum strategy is proposed, in which electron donors are tethered to the classic boron–nitrogen MR core (BCzBN) by employing an oxygen atom as a flexible anchoring point. Benefitting from the distinctive oxygen linkage and dynamic swinging behavior, the resultant MR-TADF emitters can access multiple isomeric conformations, thereby simultaneously achieving blue-shifted emission, preserved narrow full width at half maximum, enhanced quenching resistance, and faster spin flipping compared with BCzBN. As a consequence, the corresponding OLEDs achieve bright blue narrowband electroluminescence in an extremely wide doping window of 1–30 wt%, revealing a record-high external quantum efficiency of 30.4% even at 20 wt%. The results clearly highlight the great potential of the dynamic pendulum strategy for efficient blue MR-TADF emitters.

Received 7th April 2026
Accepted 8th May 2026

DOI: 10.1039/d6sc02881k

rsc.li/chemical-science

Introduction

Organic light-emitting diodes (OLEDs) have emerged as a cornerstone of modern display technologies owing to their high contrast, wide color gamut, and compatibility with flexible displays.[1–5] Nowadays, traditional fluorescent dyes, phosphorescent metal complexes, and thermally activated delayed fluorescence (TADF) emitters have been successfully developed as electroluminescent (EL) materials for OLEDs.[6–13] Among them, TADF emitters can harvest both singlet and triplet excitons in the absence of any noble metals, marking a breakthrough in high-efficiency and low-cost OLEDs.[3,14,15] However, the conventional twisted donor–acceptor (D–A) configurations, characteristic of strong charge transfer (CT) and excited-state vibrational relaxation, generally produce red-shifted and broadened spectra to deviate from the stringent color purity required for high-resolution displays.[16–22]

In 2016, Hatakeyama *et al.* revolutionized the field of TADF emitters by introducing a novel molecular design strategy based on the multiple resonance (MR) effect.[23] Such a boron–nitrogen (BN) embedded MR-TADF emitter displayed a narrowband blue emission with a full width at half maximum (FWHM) of only 28 nm and an external quantum efficiency (EQE) exceeding 20%. This pioneering work spurred extensive research into various narrowband MR-TADF derivatives.[4,24–33] For example, the classic BN core (BCzBN) acts as a key framework spanning the emission range from blue to red/deep-red, but faces two challenges (Fig. 1a).[34,35] Firstly, the planarity in BCzBN would induce strong intermolecular π–π interactions, triggering aggregation-caused quenching (ACQ) and undesirable spectral broadening in solid states. An extremely low doping concentration (<5 wt%) is often employed in device fabrication.[36–39] Thus, various strategies such as steric/conformational modulations and the "self-host" approach, which integrates host functionalities into the MR core to physically shield it, are explored to suppress ACQ and enhance the doping concentration without affecting the FWHM (Fig. 1a).[40–44] However, these approaches have almost exclusively relied on "static" spatial steric hindrance, achieved by appending rigid and bulky groups.[36,37,45–50] Secondly, although the rigid MR structure of

[a]Key Laboratory of Medicinal Chemistry for Natural Resource, Ministry of Education, School of Chemical Science and Technology, Yunnan University, National Center for International Joint Research of Photoelectronic Energy Materials and Application, Kunming 650091, P. R. China. E-mail: dingjunqiao@ynu.edu.cn; mengguoyun@ynu.edu.cn; sihan94720@outlook.com

[b]Southwest United Graduate School, Kunming 650092, P. R. China

[c]Institute of Functional Nano and Soft Materials (FUNSOM), Soochow University, Suzhou, Jiangsu, 215123, P. R. China. E-mail: xkchen@suda.edu.cn

[d]School of Physics and Astronomy, Yunnan University, Kunming 650091, P. R. China

[e]Department of Materials Science and Engineering, University of Toronto, Toronto, Ontario, Canada

[f]School of Chemical Engineering and Light Industry, Guangdong University of Technology, Guangzhou 510006, P. R. China

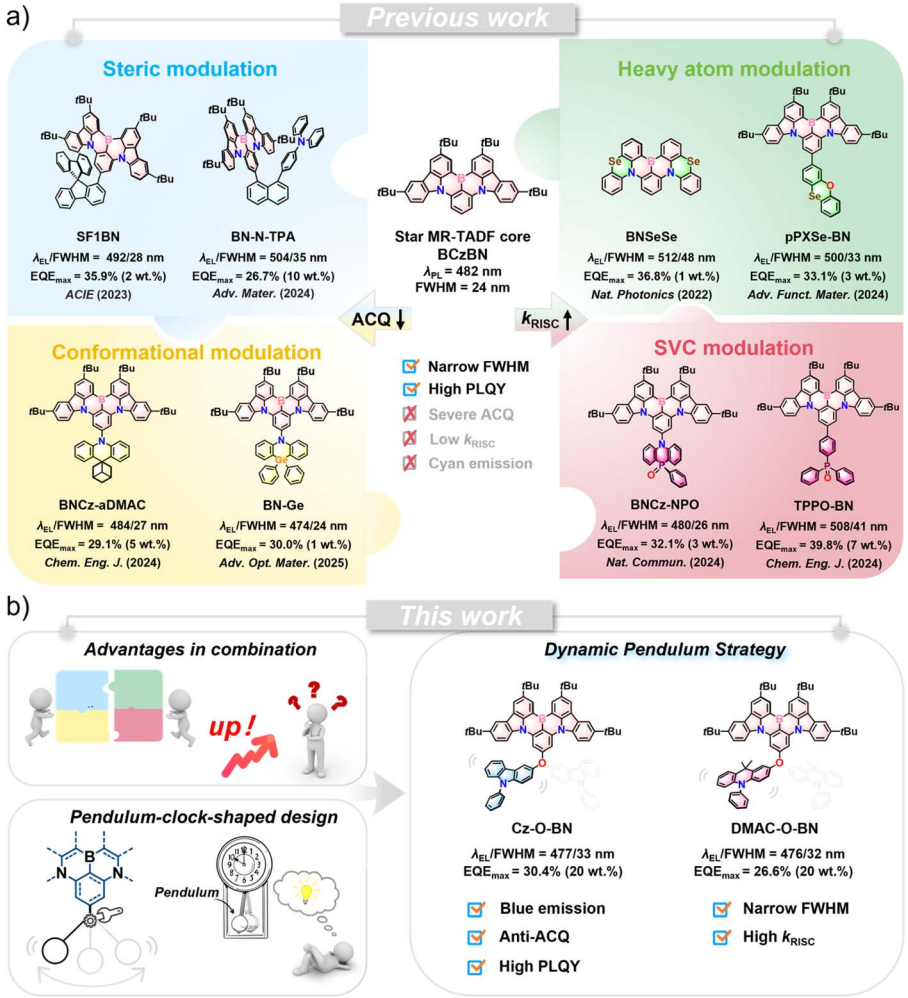

Fig. 1 Molecular design rules of MR-TADF emitters based on the BCzBN framework: (a) previously developed strategies to modulate either ACQ or k_{RISC}; (b) dynamic pendulum strategy to modulate ACQ and k_{RISC} simultaneously in this work.

BCzBN could ensure narrowband emission, its homogenized locally excited (LE) nature inevitably leads to weak spin–orbit coupling (SOC).[51] The resultant poor rate (k_{RISC}) of reverse intersystem crossing (RISC) may cause the accumulation of triplet excitons at high current density and a pronounced efficiency roll-off.[52] To solve this problem, several methods have been developed, including utilizing the heavy atom effect, promoting spin-vibration coupling (SVC),[53–56] and introducing the donor or acceptor-induced long-range CT (LRCT) character to significantly boost the RISC process without compromising color purity.[41,49,51,57]

Despite these achievements, little progress has been made in simultaneously suppressing ACQ and enhancing k_{RISC}, especially for blue MR-TADF emitters.[58] Herein, departing from the conventional wisdom of static rigidity, we are inspired by the swinging clock and propose a novel "dynamic pendulum" strategy to realize both anti-quenching and fast spin flipping for efficient blue narrowband EL (Fig. 1b). Unlike directly linked analogues, the electron donors 9-phenyl-9*H*-carbazole (Cz) and 9,9-dimethyl-10-phenyl-9,10-dihydroacridine (DMAC) are connected to the BCzBN core through a flexible oxygen bridge, yielding the blue-emitting emitters Cz-O-BN and DMAC-O-BN. Benefitting from the *para*-positioned B–π–O conjugation, their emission maxima are significantly blue-shifted to about 465 nm, while the FWHM remains almost unchanged compared with those of BCzBN ($\lambda_{max} = 482$ nm and FWHM = 24 nm). Most importantly, the electron donors in Cz-O-BN and DMAC-O-BN undergo dynamic swinging motions, allowing access to multiple isomeric conformations. In this case, not only are the intermolecular interactions expected to be modulated to suppress ACQ, but the vibrational-mode distribution is also regulated to establish favorable SVC-mediated RISC channels, thereby increasing k_{RISC} in synergy with oxygen-induced SOC. As a result, OLEDs based on Cz-O-BN exhibit efficient narrowband blue EL, maintaining high EQEs of 22.6–30.5% over a wide doping window of 1–30 wt%. Notably, a maximum EQE of 30.4% is achieved in a standard non-sensitized device, together with reduced efficiency roll-off. Considering the intrinsically challenging nature of blue emission at a high doping content of 20 wt%, this achievement sets a new performance benchmark for blue MR-TADF emitters, whereas most previously reported high-efficiency BCzBN analogues typically

emit at longer wavelengths, in the sky-blue or greenish region, under comparable doping conditions.

Results and discussion

Molecular design, synthesis, and characterization

In the molecular design of Cz-O-BN and DMAC-O-BN, the introduction of the O atom plays a pivotal and multifunctional role, which can effectively solve three long-standing challenges in this field. Unlike conventional flexible linkers that undergo uncontrolled σ-bond rotation, the sp^3-hybridized oxygen bridge enables a constrained pendulum-like conformation. Without relying on conventional rigid steric hindrance, this conformation effectively suppresses ACQ while preserving the intrinsic narrowband emission characteristics of these emitters. Meanwhile, the lone-pair electrons of the O atom and the resulting B–π–O conjugation can significantly regulate the electronic structure, realizing a substantial blue shift of the emission spectrum to the blue region and breaking the inherent limitation of sky-blue to greenish emission in the BCzBN family.[59–61] Most importantly, this integrated molecular design effectively improves the core bottleneck of high-performance materials, namely the low RISC rate of MR-TADF emitters. The oxygen lone pairs and O-bridged vibrational modes may promote SVC and facilitate singlet–triplet transitions. These synergistic effects can simultaneously address the three core problems of aggregation quenching, emission-color regulation, and slow RISC kinetics, ultimately endowing the material with excellent photophysical properties and high emission efficiency.

The synthetic routes for the developed blue MR-TADF emitters Cz-O-BN and DMAC-O-BN are outlined in Scheme S1. Starting from *para*-brominated BCzBN and hydroxylated Cz/DMAC as precursors, Ullmann condensation was performed with copper iodide and dimethylglycine hydrochloride to afford Cz-O-BN and DMAC-O-BN in acceptable yields of 20–23%. At the same time, the BN core BCzBN was synthesized as the reference for comparison. The final products were purified through column chromatography, recrystallization, and temperature-gradient vacuum sublimation in sequence before characterization and device evaluation. And their chemical structures were fully characterized by ^{1}H and ^{13}C nuclear magnetic resonance (NMR) spectroscopy, mass spectrometry, and X-ray crystallographic analysis.

The thermal properties of Cz-O-BN and DMAC-O-BN were investigated using thermogravimetric analysis and differential scanning calorimetry (Fig. S1). They show high thermal decomposition temperatures (T_d, corresponding to a 5 wt% weight loss) of 438–496 °C. The glass transition temperature (T_g)

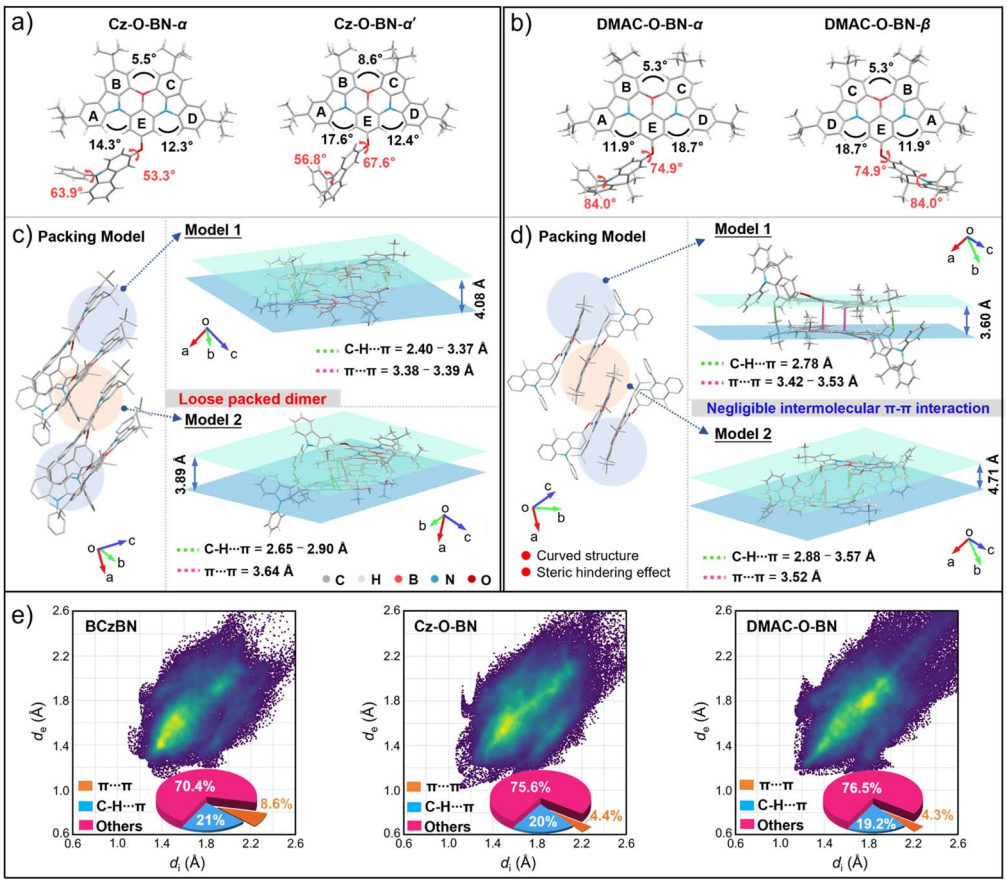

Fig. 2 (a and b) Crystal structures of Cz-O-BN-(α/α') and DMAC-O-BN-(α/β), and (c and d) their corresponding molecular packing with different models; (e) intermolecular interactions with 2D fingerprint plots defined by (d_i, d_e) pairs in Hirshfeld surface analysis of BCzBN, Cz-O-BN, and DMAC-O-BN.

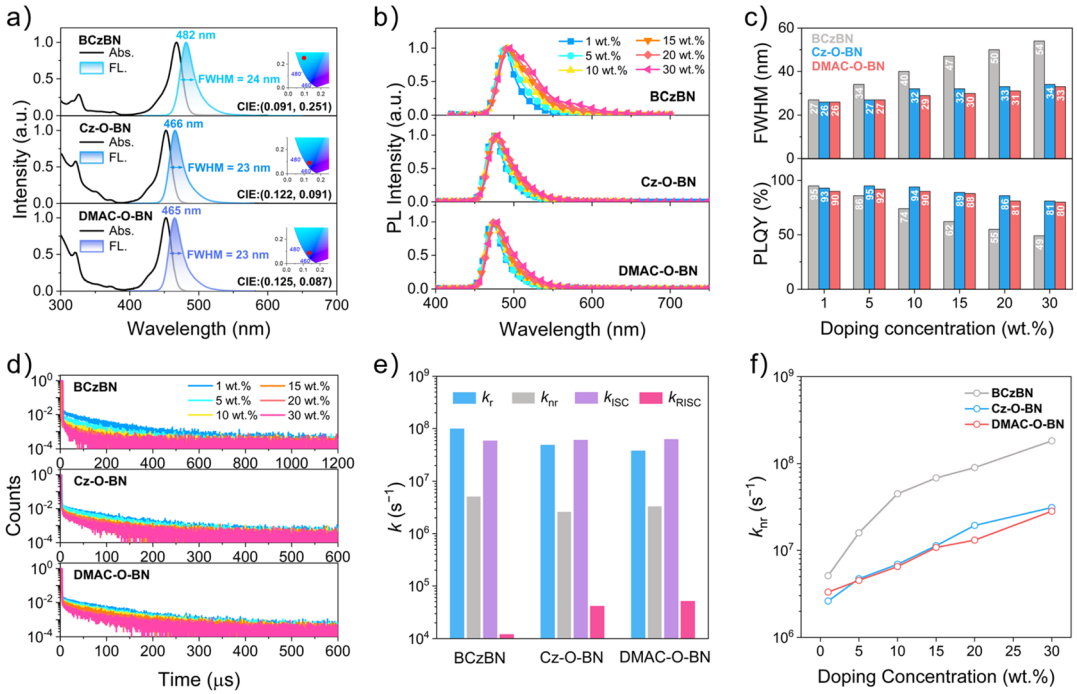

Fig. 3 Comparison of photophysical properties among BCzBN, Cz-O-BN and DMAC-O-BN: (a) UV-vis absorption and PL spectra in toluene; (b) steady-state PL spectra in doped films with varied doping ratios; (c) correlation between the FWHM and Φ_{PL} as a function of doping concentration; (d) transient PL spectra of doped films with varied doping ratios; (e) different rate constants of 1 wt% doped films; (f) relationship between k_{nr} *versus* doping concentration.

of DMAC-O-BN is 178 °C, whereas no distinct T_g is observed for Cz-O-BN. Such good thermal stability is beneficial for vacuum deposition during OLED fabrication. Moreover, cyclic voltammetry (CV) and differential pulse voltammetry (DPV) were carried out to determine the highest occupied molecular orbital (HOMO) and lowest unoccupied molecular orbital (LUMO) energy levels (Fig. S2). At a scan rate of 100 mV s^{-1}, DMAC-O-BN exhibits well-defined reversible oxidation and reduction processes, while Cz-O-BN has irreversible oxidation and reduction waves. The oxidation/reduction potentials (E_{ox}/E_{red}) of Cz-O-BN and DMAC-O-BN, taken from DPV peaks, are +0.56/−2.21 and +0.39/−2.18 V, corresponding to the HOMO/LUMO energy levels of −5.36/−2.59 and −5.19/−2.62 eV, respectively. Despite their comparable LUMO levels, DMAC-O-BN possesses a higher-lying HOMO level than Cz-O-BN owing to the stronger electron-donating ability of DMAC relative to Cz.

Single-crystal structure analysis

Single crystals of Cz-O-BN and DMAC-O-BN (Tables S1 and S2) were cultivated carefully using different solvent diffusion systems to study the influence of the dynamic pendulum groups (O-Cz/O-DMAC) on the molecular conformation and stacking behaviors. Based on their left- and right-oriented arrangements of the pendulum unit relative to the BCzBN core, the corresponding single-crystal structures are classified as α- and β-types (Fig. 2 and S3).[49] Interestingly, for Cz-O-BN, the α- and β-conformations were obtained from single crystals grown under different conditions, giving rise to four energetically favorable isomers ($\alpha/\alpha'/\beta/\beta'$). As for DMAC-O-BN, there are two isomers (α/β), in which mirror-symmetric α- and β-conformations coexist within only one unit cell. Similar to the pendulum clock, the tethered donors are able to swing freely around the anchored O atom, thus leading to polymorphism in Cz-O-BN and DMAC-O-BN.

Also, large dihedral angles (53.3–87.8°) between the O-anchored donors and the MR plane result in highly twisted structures for Cz-O-BN and DMAC-O-BN. Such a configuration gives rise to two distinct molecular stacking models (model 1 and model 2 in Fig. 2c and d), with crystal lattice interlayer separations ranging from 3.89 to 4.08 Å for Cz-O-BN and 3.60 to 4.71 Å for DMAC-O-BN. Consequently, their π–π stacking distances are in the range of 3.38–3.64 Å, exceeding the reported threshold for emission quenching (about 3.3 Å).[62] Further reduced density gradient (RDG) analysis of Cz-O-BN and DMAC-O-BN indicates the intramolecular non-covalent interactions between Cz/DMAC and the core (Fig. S4).[63] Nevertheless, according to the Hirshfeld surface analysis, both Cz-O-BN and DMAC-O-BN show fewer red isosurfaces and a substantial reduction in interchromophore contact density (especially π–π interactions) compared with BCzBN (Fig. 2e and S5).[46]

Photophysical properties

The UV-vis absorption and photoluminescence (PL) spectra were first measured at room temperature in toluene solution for Cz-O-BN and DMAC-O-BN. As shown in Fig. 3a, both compounds show a sharp absorption band centered at *ca.* 450 nm, attributable to the short-range CT (SRCT) transition of the MR core.[64] For BCzBN, a hypsochromic shift and reduced

Table 1 Summary of photophysical properties for BCzBN, Cz-O-BN, and DMAC-O-BN

Emitter	λ_{abs}[a] [nm]	λ_{em}[a] [nm]	FWHM[a] [nm/eV]	ΔE_{ST}[b] [eV]	Φ_{PL}[c] [%]	τ_p[d] [ns]	τ_d[d] [μs]	k_r[e] [10^7 s^{-1}]	k_{nr}[e] [10^6 s^{-1}]	k_{ISC}[e] [10^7 s^{-1}]	k_{RISC}[e] [10^4 s^{-1}]
BCzBN	469	482	24/0.12	0.12	95	6.2	126	9.7	5.1	5.9	1.2
Cz-O-BN	454	465	23/0.12	0.14	93	8.9	53	4.9	2.6	6.1	4.1
DMAC-O-BN	453	464	23/0.12	0.12	90	9.6	49	3.8	3.3	6.3	5.1

[a] Maximum wavelength of absorption (λ_{abs}), emission (λ_{em}), and FWHM. [b] Singlet–triplet energy gap (ΔE_{ST}) (measured in toluene). [c] Absolute photoluminescence quantum yield (Φ_{PL}). [d] Lifetimes of prompt (τ_p) and delayed (τ_d) fluorescence. [e] Rate constants of radiative decay (k_r), non-radiative decay (k_{nr}), intersystem crossing (k_{ISC}), and reverse intersystem crossing (k_{RISC}) (measured in 1 wt% doped films).

intensity are observed for Cz-O-BN and DMAC-O-BN (Fig. S6). Correspondingly, their emissive maxima upshift towards a short wavelength of 464–465 nm, accompanied by a similar FWHM of 23 nm. These observations suggest that the dynamic pendulum groups (O-Cz/O-DMAC) could effectively modulate the electronic structure of BCzBN *via* a *para*-B–π–O conjugation, but do not affect the FWHM. As verified by the solvatochromic effect (Fig. S7, S8 and Table S3), all of BCzBN, Cz-O-BN, and DMAC-O-BN depict a two-segment linear relationship in the Lippert–Mataga plots (Fig. S9). Notably, Cz-O-BN and DMAC-O-BN appear to exhibit larger excited-state dipole moments (μ_e) than BCzBN in both low- and high-polarity solvent ranges. That is, Cz-O-BN and DMAC-O-BN readily undergo charge separation to form CT states in the excited state after the incorporation of the dynamic pendulum groups (Table 1).

Subsequently, fluorescence and phosphorescence spectra were detected at 77 K (Fig. S10). And the singlet–triplet energy difference (ΔE_{ST}) of Cz-O-BN and DMAC-O-BN is estimated to be 0.14 eV and 0.12 eV, respectively, comparable to that of BCzBN (0.12 eV). The small ΔE_{ST} is expected to endow them with efficient delayed fluorescence. Therefore, Cz-O-BN and DMAC-O-BN are dispersed into a high-energy-gap host 9-(2-(9-phenyl-9*H*-carbazol-3-yl)phenyl)9*H*-3,9′-bicarbazole (PhCzBCz) at a 1 wt% doping concentration to investigate their photophysical properties (Fig. S11–S14). The characteristic temperature dependence and oxygen quenching behavior confirm the TADF nature of Cz-O-BN and DMAC-O-BN. Their doped films emit bright blue PL and show obvious delayed components, with delayed lifetimes (τ_d) of 53 and 49 μs, respectively. Compared with BCzBN (126 μs), the reduced τ_d is reasonably ascribed to the favored RISC process, which originates from the dynamic pendulum O-Cz/O-DMAC. In fact, the k_{RISC} is greatly increased from 1.2×10^4 s^{-1} for BCzBN to 4.1×10^4 s^{-1} for Cz-O-BN and 5.1×10^4 s^{-1} for DMAC-O-BN (Fig. 3e).

Finally, the effect of O-Cz/O-DMAC on anti-quenching is explored in detail by delicately tuning the doping content. It is found that Cz-O-BN and DMAC-O-BN display less concentration dependence on the steady-state and transient PL relative to BCzBN (Fig. 3b, d and S15). With increasing doping concentration from 1 wt% to 30 wt%, the BCzBN spectrum progressively broadened, with an additional shoulder emerging at 584 nm. The corresponding FWHM is significantly up from 27 nm to 54 nm, while the PL quantum yield (Φ_{PL}) is down from 95% to 49% (Fig. 3c, Tables S4 and S5). The strong ACQ and enhanced non-radiative decay (Fig. 3f) may be responsible for the spectral broadening and decreased Φ_{PL}. By contrast, Cz-O-BN and DMAC-O-BN retain a sharp PL linewidth and good resistance to the ACQ, accompanied by a slightly varied FWHM in the range of 26–34 nm and Φ_{PL} in the range of 80–93%. In agreement with the above-mentioned crystallographic analysis, the remarkable anti-quenching ability of Cz-O-BN and DMAC-O-BN arises from the dynamic pendulum groups, which can effectively suppress the formation of emissive excimers and aggregates. This is further supported by the PL behavior observed in a tetrahydrofuran/water mixture. Different from the continuously decreased PL for BCzBN, the intensity of Cz-O-BN and DMAC-O-BN steadily increases with the increasing water fractions (f_w), while the FWHM remains remarkably stable at $f_w \leq 60\%$ (Fig. S16).[65]

Theoretical simulation

To gain a deep insight into the structural and electronic characteristics of Cz-O-BN and DMAC-O-BN, density functional theory (DFT) calculations were conducted at the B3LYP/6-31G(d) level. It is found that their HOMO and LUMO predominantly reside on the BCzBN core, suggesting that the intrinsic MR characteristics are well preserved (Fig. 4a). Compared with BCzBN, the LUMO distribution is further delocalized onto the anchored O atom for Cz-O-BN and DMAC-O-BN, leading to the elevated electrochemical bandgap and thus blue-shifted PL. This observation is consistent with the extended negative potentials from the core to the O atom because of the *para*-positioned B–π–O conjugation (Fig. S18). Meanwhile, the electron-donating capability of the dynamic pendulum groups makes HOMO-1 migrate from the BCzBN core to O-Cz/O-DMAC (Fig. S17). Such a frontier molecular orbital (FMO) distribution is believed to enhance CT in excited states, consistent with the solvatochromic effect and energy difference between vacuum and CH_2Cl_2 environments (Fig. S19).[66]

On one hand, natural transition orbital (NTO) analysis[67] was performed based on a STEOM-DLPNO-CCSD/def2-TZVP level compared with B3LYP/6-31G(d) (Fig. S20–S24). It is found that the advanced STEOM-DLPNO-CCSD calculation with two-electron excitations has demonstrated much more accuracy for Cz-O-BN and DMAC-O-BN. The estimated S_1–T_1 energy gaps of 0.22–0.24 eV substantially reduce the apparent discrepancy with the experimental values (ΔE_{ST} = 0.12–0.14 eV). Unlike the SRCT of BCzBN, both Cz-O-BN and DMAC-O-BN present SRCT

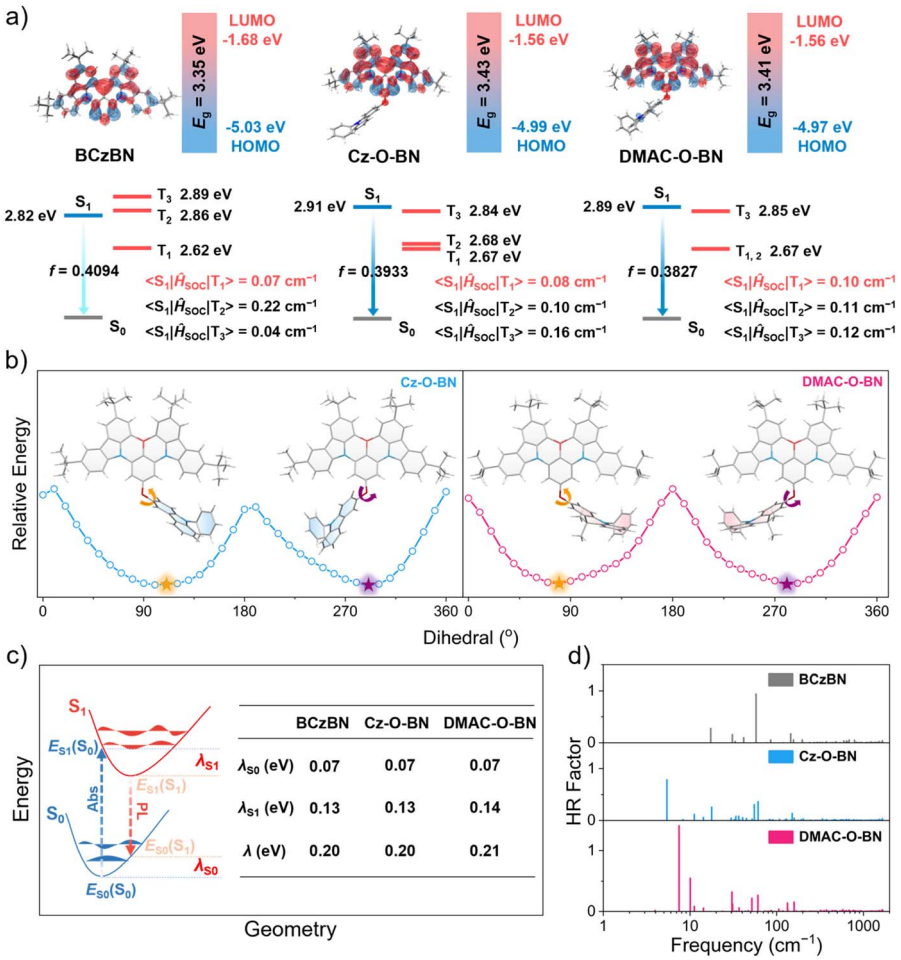

Fig. 4 Theoretical simulation for Cz-O-BN and DMAC-O-BN compared with BCzBN: (a) taking the α-type single crystal as an example, the HOMO/LUMO distribution and band gap (E_g) were calculated at the B3LYP/6-31G(d) level, and the singlet/triplet energy levels and SOCMEs between S_1 and T_n ($n = 1$–3) were calculated at the STEOM-DLPNO-CCSD/def2-TZVP level; (b) PES scans and conformational structures of the ground states; (c) theoretical estimation of the total reorganization energies (λ); (d) the Huang–Rhys (HR) factor for the $S_1 \rightarrow S_0$ transition.

mixed with LRCT in certain high-lying excited states. Consequently, they exhibit a little larger SOC matrix elements (SOCMEs) between the first singlet state (S_1) and triplet state (T_1) than that of BCzBN (0.07 cm^{-1}). With an α-type single crystal as an example, the S_1-to-T_1 SOCME is gently increased to 0.08 cm^{-1} for Cz-O-BN and 0.10 cm^{-1} for DMAC-O-BN (Fig. 4a), indicative of the favored SOC effect to some degree from the oxygen's lone pairs. As discussed above, such a small SOCME improvement does not match the k_{RISC} enhancement (about 3–4 times).

On the other hand, one-dimensional flexible potential energy surface (PES) scans were performed to assess the conformational energy landscape for Cz-O-BN and DMAC-O-BN. When the dihedral angle between the MR core and O-anchored donor changes, the PES depicts two distinct low-lying regions with local energy minima, corresponding to the α-type and β-type conformations (Fig. 4b). And the relatively broad energy valleys mean the existence of multiple conformers with comparable potential energies.[42,43,49] According to the Boltzmann distribution at ambient temperature, their α- and β-type conformers coexist in approximately equal proportions, which can well explain their polymorphism in single crystals. The conformational diversity enabled by the flexible ether linkage suggests, at this stage, that the dynamic pendulum groups O-Cz/O-DMAC may enable Cz-O-BN and DMAC-O-BN to access multiple isomeric conformations. Therefore, beyond the oxygen-induced SOC enhancement, the conformational flexibility of O-Cz/O-DMAC may regulate the excited-state energy levels and vibrational modes, thereby promoting vibronically assisted singlet–triplet crossing and facilitating SVC-mediated RISC (Fig. S25).[56,68] That is, both oxygen-induced SOC and flexibility-induced nonadiabatic SVC contribute to the increased k_{RISC}.[23] This conformational-regulation mechanism is supported by thermodynamic and photophysical evidence. The RISC activation energies of Cz-O-BN and DMAC-O-BN are both ~0.07 eV (Fig. S13), markedly lower than their experimentally determined ΔE_{ST} values of 0.12–0.14 eV, indicating vibronically assisted crossing rather than a purely classical thermally activated T_1-to-S_1 process. Moreover, the stronger deoxygenation-induced PL response in dilute solution than in doped films is consistent with greater conformational freedom in solution,

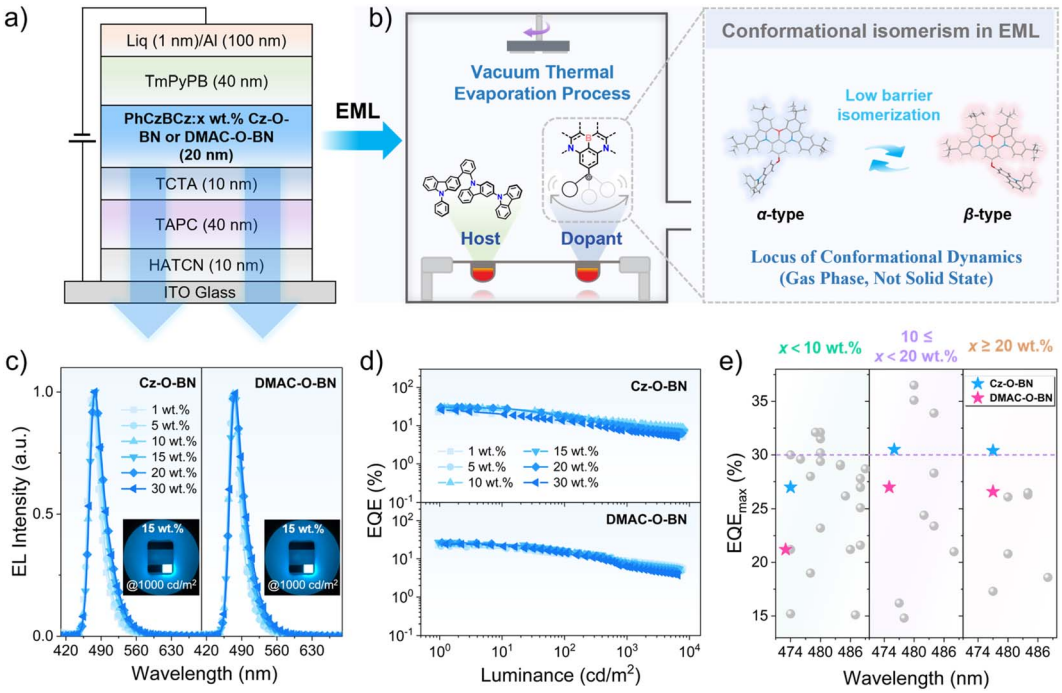

Fig. 5 Device fabrication and performance for Cz-O-BN and DMAC-O-BN: (a) architecture of the device; (b) mechanism of conformational isomerization in the EML (Cz-O-BN as a representative example); (c) EL spectra at 1000 cd m^{-2} at varied doping concentrations; (d) EQE as a function of luminance at varied doping concentrations; (e) EQE comparison of blue-emitting MR-TADF emitters across different doping concentration ranges (blue MR-TADF emitters peaking at 470–490 nm).

where torsional motions and vibrational relaxation can facilitate SVC-mediated RISC, while the rigid host matrix partially suppresses this contribution (Fig. S14).

To further investigate the impact of O-Cz/O-DMAC on the structural relaxation between the excited and ground states, we employed the MOMAP software to calculate and analyze the reorganization energy (λ) and Huang–Rhys (HR) factors.[69] As can be seen in Fig. 4c, the λ values (0.20 eV for Cz-O-BN and 0.21 eV for DMAC-O-BN) are comparable to that of BCzBN (0.20 eV), suggesting similar degrees of geometric relaxation upon de-excitation. The HR factor, which quantifies the strength of electron-vibration coupling during electronic transitions such as $S_1 \rightarrow S_0$, reveals that the introduced O-Cz and O-DMAC units reduce the contribution of high-frequency vibrational modes while enhancing that of low-frequency modes (Fig. 4d). For instance, Cz-O-BN exhibits two prominent low-frequency twisting vibrational modes at 5.41 cm^{-1} (HR factor = 0.78) and 60.98 cm^{-1} (HR factor = 0.36), while DMAC-O-BN displays modes at 7.47 cm^{-1} (HR factor = 1.41) and 10.05 cm^{-1} (HR factor = 0.55) (Fig. S26 and S27). Thereby, Cz-O-BN and DMAC-O-BN can effectively preserve the narrowband emission of the parent BCzBN core.[34]

Additionally, the spin-density distributions (TSDDs) of the lowest excited triplet state (T_1) were analyzed for Cz-O-BN and DMAC-O-BN. Their triplet states are found to be completely localized on the MR core, and O-Cz/O-DMAC tend to act as the periphery encapsulated groups (Fig. S28). From BCzBN to Cz-O-BN and DMAC-O-BN, the molecular dimensions along the x, y, and z axes increase from 22.0/13.7/8.7 to 22.6/18.9/11.5 and 22.9/19.2/11.5 Å, respectively (Fig. S29). Consistent with the single-crystal stacking, the increased steric hindrance is expected to enlarge the separation between the MR core and adjacent molecules, thereby suppressing ACQ and endowing Cz-O-BN and DMAC-O-BN with enhanced quenching resistance.

Device performance

It should be noted that a typical vacuum thermal evaporation is used to prepare doped films for the above-mentioned photophysical measurements, followed by OLED fabrication (Fig. 5a and b). We therefore infer that the dynamical swinging may be activated during thermal deposition *via* a solid–gas–solid phase transition. In this case, a multiple conformational ensemble could be generated and subsequently immobilized within the densely packed films. As a result, the blue-shifted emission, unaffected FWHM, good anti-quenching, and fast spin flipping are observed in the PL process owing to the dynamic pendulum architecture of Cz-O-BN and DMAC-O-BN.

To further validate such advantages in the EL process, their OLEDs are fabricated with a device structure of indium tin oxide (ITO)/hexaazatriphenylenehexacabonitrile (HATCN) (10 nm)/1,1-bis((di-4-tolylamino)phenyl)-cyclohexane (TATC) (40 nm)/tris(4-carbazoyl-9-ylphenyl)amine (TCTA) (10 nm)/EML (20 nm)/1,3,5-tri(*m*-pyrid-3-ylphenyl)benzene (TmPyPB) (40 nm)/liq (1 nm)/Al (Fig. 5a and S30). Here, the emissive layer (EML) consists of a binary host-guest system, in which Cz-O-BN and DMAC-O-BN are doped into PhCzBCz at concentrations ranging from 1 wt% to 30 wt%. And PhCzBCz is selected as the host due

Table 2 Device performance for Cz-O-BN and DMAC-O-BN

Emitter	Doping content [wt%]	V_{on}[a] [V]	L_{max}[b] [cd m^{-2}]	CE[c] [cd A^{-1}]	PE[c] [lm W^{-1}]	EQE[c] [%]	λ_{EL}[d] [nm]	FWHM[e] [nm]	CIE[e] (x, y)
Cz-O-BN	1	3.1	7875	30.5	30.9	22.6	472	27	(0.12, 0.18)
	5	3.0	8436	36.9	38.3	27.0	474	28	(0.11, 0.18)
	10	3.0	8277	43.3	45.6	30.0	475	30	(0.11, 0.21)
	15	2.9	8191	49.8	55.3	30.5	476	32	(0.11, 0.24)
	20	2.9	7602	51.1	50.3	30.4	477	33	(0.11, 0.26)
	30	3.0	6352	45.2	42.8	25.4	477	34	(0.11, 0.27)
DMAC-O-BN	1	3.2	8329	26.3	26.8	19.9	471	27	(0.12, 0.17)
	5	3.1	7473	27.5	27.6	21.2	473	27	(0.11, 0.16)
	10	3.1	7208	34.7	35.1	24.9	474	29	(0.11, 0.20)
	15	3.0	6884	37.8	39.6	27.0	475	30	(0.11, 0.21)
	20	3.0	6710	39.5	41.4	26.6	476	32	(0.11, 0.23)
	30	3.0	6756	39.2	41.2	24.2	476	33	(0.11, 0.26)

[a] Turn-on voltage at 1 cd m^{-2}. [b] Maximum luminance. [c] Data at maximum. [d] Peak EL wavelength. [e] Measured at 1000 cd m^{-2}. CE: current efficiency; PE: power efficiency; EQE: external quantum efficiency; FWHM: full width at half maximum.

to its balanced charge transport, appropriate singlet/triplet energy levels, and well-matched HOMO/LUMO with the dopants.[70]

At a low doping concentration of 1 wt%, Cz-O-BN and DMAC-O-BN realize a maximum EQE of 19.9–22.6%, comparable to that of BCzBN (21.3% in Fig. S31 and Table S6). Despite this, the efficiency roll-off at 1000 cd m^{-2} is distinctly reduced from 74% for BCzBN to 57–59% for Cz-O-BN and DMAC-O-BN, due to the accelerated RISC process. Additionally, the EL peak is blue-shifted from 489 nm to 471–472 nm while maintaining an unchanged FWHM of 27 nm, and the corresponding Commission Internationale de l'Éclairage (CIE) coordinates shift from (0.09, 0.38) to (0.12, 0.17–0.18). This trend illustrates that incorporating dynamic pendulum groups can modulate the emission color of BCzBN toward shorter wavelengths while maintaining its narrow FWHM (Table 2).

As the doping concentration increases from 1 wt% to 30 wt%, the FWHM of BCzBN-based devices is dramatically broadened from 27 to 54 nm, together with a bathochromic shift. Nevertheless, the unwanted spectral red shift and broadening are considerably suppressed for Cz-O-BN and DMAC-O-BN (Fig. 5c and S32). For example, the EL peaks and FWHMs of Cz-O-BN-based devices vary within narrow ranges of 472–477 nm and 27–34 nm, respectively. The difference between BCzBN and Cz-O-BN/DMAC-O-BN in EL behavior is consistent with their PL characteristics, indicating improved resistance to concentration quenching, which is further validated by the non-doped device results (Fig. S33 and Table S7). As a result, Cz-O-BN achieves the best device performance, achieving high EQEs of 22.6–30.5% over an extremely wide doping window of 1–30 wt%. Specifically, a state-of-the-art EQE of 30.4% is retained even at a high doping concentration of 20 wt%. To our knowledge, such a performance is among the highest ever reported for blue MR-TADF emitters (Fig. 5e and Table S9), highlighting the superiority of the dynamic pendulum strategy (Fig. 5b).

Subsequently, we conducted a preliminary lifetime test on the unencapsulated devices with 5 wt% doping of Cz-O-BN and DMAC-O-BN. Under constant-current operation at an initial luminance of 500 cd m^{-2}, they exhibit LT50 lifetimes of approximately 27 h and 21 h, respectively (Fig. S34). Meanwhile, iridium(III)bis[2-(4,6-difluorophenyl)pyridyl-N,C2′]picolinate (FIrpic) was selected as the sensitizer to enhance exciton utilization and further optimize the device efficiency. As shown in Fig. S35–S38, the absorption spectra of Cz-O-BN and DMAC-O-BN exhibit pronounced overlap with the PL spectrum of FIrpic in toluene, indicating favorable spectral matching for Förster resonance energy transfer from FIrpic to the emitters. For example, Cz-O-BN achieves an improved EQE of up to 33.7% even at a low doping concentration of 2 wt% (Fig. S39 and Table S8). Notably, a small efficiency roll-off is also observed, with the EQE remaining as high as 25.4% at 1000 cd m^{-2}.

Conclusions

In summary, a novel dynamic pendulum strategy has been proposed to design efficient blue MR-TADF emitters, namely Cz-O-BN and DMAC-O-BN. Compared with the BCzBN prototype, they not only exhibit bright blue-shifted narrowband PL due to the *para*-conjugated oxygen linkage, but also adopt multiple isomeric conformations enabled by the pendulum-like motion of the O-Cz and O-DMAC groups. Consequently, both anti-quenching and fast spin flipping are achieved simultaneously in Cz-O-BN and DMAC-O-BN, thus endowing their OLEDs with a wide doping window of 1–30 wt%. For example, Cz-O-BN maintains a promising EQE of up to 30.4% even at a high doping concentration of over 20 wt%. We believe this work helps achieve a new efficiency milestone and will shed light on the development of high-performance blue MR-TADF emitters with minimal reliance on doping concentration.

Author contributions

X. G., G. M. and J. D. conceived the idea and designed the experiments. X. G. performed the synthesis and basic property characterization, and drafted the manuscript. X. G. and N. S.

performed the fabrication and characterization of the devices. X. G., B. C., J.-Q. L. and X.-K. C. carried out the theoretical calculations. H. S. assisted in characterization and data analysis. G. M., L. D., Z.-H. L. and J. D. reviewed and edited the manuscript. All authors contributed to the manuscript and participated in the discussion of the results.

Conflicts of interest

The authors declare no conflict of interest.

Data availability

The data supporting this article have been included as part of the supplementary information (SI). Supplementary information is available. See DOI: https://doi.org/10.1039/d6sc02881k.

CCDC 2414854 for Cz-O-BN-(α/α′), 2414856 for Cz-O-BN-(β/β′) and 2414857 for DMAC-O-BN-(α/β) contain the supplementary crystallographic data for this paper.[71a–c]

Acknowledgements

The authors acknowledge the financial support from the National Natural Science Foundation of China (No. 52303253 and 52273198), Yunnan Fundamental Research Projects (No. 202501CF070071 and 202301BF070001-008), and the Yunling Scholar Project of "Yunnan Revitalization Talent Support Program". We also thank the Advanced Analysis and Measurement Center of Yunnan University for the assistance with instrumentation. X. Gan acknowledges the Graduate Research Program of Yunnan University (No. KC-24248970 and KC-252511770). And Dr N. Sun acknowledges the Yunnan Province Basic Research Project (No. 202301AT070221).

Notes and references

1 C. W. Tang and S. A. VanSlyke, *Appl. Phys. Lett.*, 1987, **51**, 913–915.
2 G. Hong, X. Gan, C. Leonhardt, Z. Zhang, J. Seibert, J. M. Busch and S. Brase, *Adv. Mater.*, 2021, **33**, 2005630.
3 H. Uoyama, K. Goushi, K. Shizu, H. Nomura and C. Adachi, *Nature*, 2012, **492**, 234–238.
4 X. Wu, S. Ni, C. H. Wang, W. Zhu and P. T. Chou, *Chem. Rev.*, 2025, **125**, 6685–6752.
5 J. M. Ha, S. H. Hur, A. Pathak, J.-E. Jeong and H. Y. Woo, *NPG Asia Mater.*, 2021, **13**, 53.
6 J. Wang, Y. Niu, Y. Jiang, C. Yao, Z. Dai, Y. Deng and J. Zhang, *Chem. Eng. J.*, 2025, **524**, 169199.
7 X. Feng, X. Wang, C. Redshaw and B. Z. Tang, *Chem. Soc. Rev.*, 2023, **52**, 6715–6753.
8 Y. C. Wei, K. H. Kuo, Y. Chi and P. T. Chou, *Acc. Chem. Res.*, 2023, **56**, 689–699.
9 T. Y. Li, S. J. Zheng, P. I. Djurovich and M. E. Thompson, *Chem. Rev.*, 2024, **124**, 4332–4392.
10 X. Li, L. Yan, S. Liu, S. Wang, J. Rao, L. Zhao, H. Tian, J. Ding and L. Wang, *Angew. Chem., Int. Ed.*, 2023, **62**, e202300529.
11 J. Wang, Y. Yang, F. Gu, X. Zhai, C. Yao, J. Zhang, C. Jiang and X. Xi, *ACS Appl. Mater. Interfaces*, 2023, **15**, 59643–59654.
12 J. Sun, H. Ahn, S. Kang, S.-B. Ko, D. Song, H. A. Um, S. Kim, Y. Lee, P. Jeon, S.-H. Hwang, Y. You, C. Chu and S. Kim, *Nat. Photonics*, 2022, **16**, 212–218.
13 A. Farokhi, S. Lipinski, L. M. Cavinato, H. Shahroosvand, B. Pashaei, S. Karimi, S. Bellani, F. Bonaccorso and R. D. Costa, *Chem. Soc. Rev.*, 2025, **54**, 266–340.
14 H. Nakanotani, T. Higuchi, T. Furukawa, K. Masui, K. Morimoto, M. Numata, H. Tanaka, Y. Sagara, T. Yasuda and C. Adachi, *Nat. Commun.*, 2014, **5**, 4016–4023.
15 K. Suzuki and H. Kaji, *J. Am. Chem. Soc.*, 2023, **145**, 16324–16329.
16 Q. Zhang, J. Li, K. Shizu, S. Huang, S. Hirata, H. Miyazaki and C. Adachi, *J. Am. Chem. Soc.*, 2012, **134**, 14706–14709.
17 Q. Zhang, B. Li, S. Huang, H. Nomura, H. Tanaka and C. Adachi, *Nat. Photonics*, 2014, **8**, 326–332.
18 Y. Z. Shi, K. Wang, X. Li, G. L. Dai, W. Liu, K. Ke, M. Zhang, S. L. Tao, C. J. Zheng, X. M. Ou and X. H. Zhang, *Angew. Chem., Int. Ed.*, 2018, **57**, 9480–9484.
19 Y. H. He, F. M. Xie, K. Zhang, D. Yang, Y. Shen, H. Z. Li, D. Ma, Y. Q. Li and J. X. Tang, *Adv. Funct. Mater.*, 2023, **33**, 2304006.
20 J. Wang, Y. Yang, C. Jiang, M. He, C. Yao and J. Zhang, *J. Mater. Chem. C*, 2022, **10**, 3163–3171.
21 M. Kim, S. K. Jeon, S. H. Hwang and J. Y. Lee, *Adv. Mater.*, 2015, **27**, 2515–2520.
22 J.-R. Wu, Y.-J. Yang, H.-T. Yuan, S.-J. Ge, Y.-K. Qu, H.-X. Jiang, Y. Liu, D.-Y. Zhou, L.-S. Liao and Z.-Q. Jiang, *Chem. Sci.*, 2026, **17**, 5638–5647.
23 T. Hatakeyama, K. Shiren, K. Nakajima, S. Nomura, S. Nakatsuka, K. Kinoshita, J. Ni, Y. Ono and T. Ikuta, *Adv. Mater.*, 2016, **28**, 2777–2781.
24 Y. Kondo, K. Yoshiura, S. Kitera, H. Nishi, S. Oda, H. Gotoh, Y. Sasada, M. Yanai and T. Hatakeyama, *Nat. Photonics*, 2019, **13**, 678–682.
25 M. Mamada, M. Hayakawa, J. Ochi and T. Hatakeyama, *Chem. Soc. Rev.*, 2024, **53**, 1624–1692.
26 Y. Li, X. Tan, B. Cai and C. Y. Chan, *Adv. Opt. Mater.*, 2025, **13**, 2403556.
27 Q. Feng, Y. Zhou, H. Xu, J. Liu, Z. Wan, Y. Wang, P. Yang, S. Ye, Y. Zhang, X. Cao, D. Cao and H. Huang, *Chem. Soc. Rev.*, 2025, **54**, 5995–6061.
28 F. Ni, Y. Huang, L. Qiu and C. Yang, *Chem. Soc. Rev.*, 2024, **53**, 5904–5955.
29 P. Keerthika and R. K. Konidena, *Adv. Opt. Mater.*, 2023, **11**, 2301732.
30 H. Jiang, J. Jin and W. Y. Wong, *Adv. Funct. Mater.*, 2023, **33**, 2306880.
31 X. Fan, X. Hao, F. Huang, J. Yu, K. Wang and X. Zhang, *Adv. Sci.*, 2023, **10**, 2303504.
32 S. M. Suresh, D. Hall, D. Beljonne, Y. Olivier and E. Zysman-Colman, *Adv. Funct. Mater.*, 2020, **30**, 1908677–1908702.
33 W. C. Guo, W. L. Zhao, K. K. Tan, M. Li and C. F. Chen, *Angew. Chem., Int. Ed.*, 2024, **63**, e202401835.
34 Y. Xu, Z. Cheng, Z. Li, B. Liang, J. Wang, J. Wei, Z. Zhang and Y. Wang, *Adv. Opt. Mater.*, 2020, **8**, 1902142–1902149.

35 Y. Zhang, D. Zhang, J. Wei, X. Hong, Y. Lu, D. Hu, G. Li, Z. Liu, Y. Chen and L. Duan, *Angew. Chem., Int. Ed.*, 2020, **59**, 17499–17503.
36 P. Jiang, J. Miao, X. Cao, H. Xia, K. Pan, T. Hua, X. Lv, Z. Huang, Y. Zou and C. Yang, *Adv. Mater.*, 2022, **34**, 2106954.
37 Y. Zhang, J. Wei, D. Zhang, C. Yin, G. Li, Z. Liu, X. Jia, J. Qiao and L. Duan, *Angew. Chem., Int. Ed.*, 2022, **61**, e202113206.
38 Y. K. Qu, D. Y. Zhou, F. C. Kong, Q. Zheng, X. Tang, Y. H. Zhu, C. C. Huang, Z. Q. Feng, J. Fan, C. Adachi, L. S. Liao and Z.-Q. Jiang, *Angew. Chem., Int. Ed.*, 2022, **61**, e202201886.
39 S. J. Wu, X. F. Fu, D. H. Zhang, Y. F. Sun, X. Lu, F. L. Lin, L. Meng, X. L. Chen and C. Z. Lu, *Adv. Mater.*, 2024, **36**, 2401724.
40 J. Bian, S. Chen, L. Qiu, R. Tian, Y. Man, Y. Wang, S. Chen, J. Zhang, C. Duan, C. Han and H. Xu, *Adv. Mater.*, 2022, **34**, 2110547.
41 S. Chen, Y. Wang, J. Lin, R. Tian, S. Li, Y. Man, S. Chen, J. Zhang, C. Duan, C. Han and H. Xu, *Chem. Eng. J.*, 2024, **489**, 151517.
42 H. Wu, Y.-Z. Shi, M.-Y. Li, X.-C. Fan, F. Huang, K. Wang, J. Yu and X.-H. Zhang, *Chem. Eng. J.*, 2024, **480**, 147977.
43 S. J. Li, X. Tang, C. H. Ng, J. Y. Lim, W. K. Tang, W. C. Chen, Y. Huo, M. Ng, S. S. Chen, D. Zhang, L. Duan and M. C. Tang, *Adv. Opt. Mater.*, 2025, **13**, 2402479.
44 Y. Feng, Y. Xu, C. Qu, Q. Wang, K. Ye, Y. Liu and Y. Wang, *Adv. Mater.*, 2024, **36**, 2403061.
45 D. Jiang, H. Sasabe, Y. Chen, Y. Sagae, H. Sato, D. Yokoyama, H. Katagiri and J. Kido, *Adv. Mater.*, 2025, **37**, 2409746.
46 J. M. Jin, D. Liu, W. C. Chen, C. Shi, G. Chen, X. Wang, L. Xing, W. Ying, S. Ji, Y. Huo and S. J. Su, *Angew. Chem., Int. Ed.*, 2024, **63**, e202401120.
47 X.-Q. Gan, Z.-M. Ding, D.-H. Liu, W.-Q. Zheng, B. Ma, H. Zhang, X. Chang, L. Wang, Y. Liu, X. Wu, S.-J. Su and W. Zhu, *Adv. Opt. Mater.*, 2023, **11**, 2300195.
48 C. Qu, Y. Wu, L. Duan and Y. Zhang, *Angew. Chem., Int. Ed.*, 2026, e3968771.
49 L. Xing, J. Wang, W. C. Chen, B. Liu, G. Chen, X. Wang, J. H. Tan, S. S. Chen, J. X. Chen, S. Ji, Z. Zhao, M. C. Tang and Y. Huo, *Nat. Commun.*, 2024, **15**, 6175.
50 X. Wang, J. Chen, S. Ni, Y. Hu, H. Dai, Z. Xiao, W. Zhu, P.-T. Chou and X. Wu, *Chem. Sci.*, 2026, **17**, 6702–6709.
51 Z. Huang, H. Xie, J. Miao, Y. Wei, Y. Zou, T. Hua, X. Cao and C. Yang, *J. Am. Chem. Soc.*, 2023, **145**, 12550–12560.
52 L. Wu, X. Mu, D. Liu, W. Li, D. Li, J. Zhang, C. Liu, T. Feng, Y. Wu, J. Li, S. J. Su and Z. Ge, *Angew. Chem., Int. Ed.*, 2024, **63**, e202409580.
53 Y. X. Hu, J. Miao, T. Hua, Z. Huang, Y. Qi, Y. Zou, Y. Qiu, H. Xia, H. Liu, X. Cao and C. Yang, *Nat. Photonics*, 2022, **16**, 803–810.
54 Z. Chen, D. Liu, M. Li, Y. Jiao, Z. Yang, K. Liu and S. J. Su, *Adv. Funct. Mater.*, 2024, **34**, 2404278.
55 I. S. Park, H. Min and T. Yasuda, *Angew. Chem., Int. Ed.*, 2022, **61**, e202205684.
56 H. L. Lee, S. O. Jeon, I. Kim, S. C. Kim, J. Lim, J. Kim, S. Park, J. Chwae, W. J. Son, H. Choi and J. Y. Lee, *Adv. Mater.*, 2022, **34**, 2202464.
57 Q. Li, H. Zhao, M. Li, Y. Liu, S. Yan and Z. Ren, *Angew. Chem., Int. Ed.*, 2025, **64**, e202506654.
58 R. Z. An, F. M. Zhao, C. Shang, M. Zhou and L. S. Cui, *Angew. Chem., Int. Ed.*, 2025, **64**, e202420489.
59 L. Xu, Y. Mo, N. Su, C. Shi, N. Sun, Y. Zhang, L. Duan, Z. H. Lu and J. Ding, *Nat. Commun.*, 2023, **14**, 1678.
60 M. Yang, I. S. Park and T. Yasuda, *J. Am. Chem. Soc.*, 2020, **142**, 19468–19472.
61 G. Meng, H. Dai, Q. Wang, J. Zhou, T. Fan, X. Zeng, X. Wang, Y. Zhang, D. Yang, D. Ma, D. Zhang and L. Duan, *Nat. Commun.*, 2023, **14**, 2394.
62 Y. Fu, H. Liu, B. Z. Tang and Z. Zhao, *Adv. Funct. Mater.*, 2024, **34**, 2401434.
63 X. Xiong, J. Q. Li, T. F. Chen, X. C. Fan, Y. C. Cheng, H. Wang, F. Huang, H. Wu, J. Yu, X. K. Chen, K. Wang and X. H. Zhang, *Adv. Funct. Mater.*, 2024, **34**, 2313726.
64 S. Wu, D. Chen, X. H. Zhang, D. Sun and E. Zysman-Colman, *Adv. Mater.*, 2025, **37**, 2415289.
65 R.-J. Wang, F. Zheng, J. Hu, Y.-L. Wu, X.-L. Liu, J.-X. Chen, L. Xing, Q.-E. Wu, Y. Huo and W.-C. Chen, *Chem. Eng. J.*, 2025, **514**, 163327.
66 J. Jin, M. Chen, H. Jiang, B. Zhang, Z. Xie and W.-Y. Wong, *ACS Mater. Lett.*, 2024, **6**, 3246–3253.
67 T. Lu and F. Chen, *J. Comput. Chem.*, 2012, **33**, 580–592.
68 V. V. Patil, H. L. Lee, I. Kim, K. H. Lee, W. J. Chung, J. Kim, S. Park, H. Choi, W. J. Son, S. O. Jeon and J. Y. Lee, *Adv. Sci.*, 2021, **8**, 2101137.
69 Z. Shuai, *Chin. J. Chem.*, 2020, **38**, 1223–1232.
70 Y. Qu, Y. Xu, T. Huang, X. Song, K. Ye and Y. Wang, *Angew. Chem., Int. Ed.*, 2025, **64**, e202506201.
71 (*a*) CCDC 2414854: Experimental Crystal Structure Determination, 2026, DOI: 10.5517/ccdc.csd.cc2m1vj2.; (*b*) CCDC 2414856: Experimental Crystal Structure Determination, 2026, DOI: 10.5517/ccdc.csd.cc2m1vl4; (*c*) CCDC 2414857: Experimental Crystal Structure Determination, 2026, DOI: 10.5517/ccdc.csd.cc2m1vm5.